IEEE Robotics and Automation Letters (RAL) paper presented at
2024 IEEE/RSJ International Conference on Intelligent Robots and Systems (IROS)
October 14-18, 2024. Abu Dhabi, UAE

A Magnetic Helical Miniature Robot With Soft Magnetic-Controlled Gripper

Aoji Zhu, *Graduate Student Member, IEEE*, Chenyao Bai, *Member, IEEE*, Xiwen Lu, *Student Member, IEEE*, Yunlong Zhu, Kezhi Wang, *Senior Member, IEEE*, and Jiarui Zhu

***Abstract*—Magnetic helical miniature robots (MHMRs) exhibit efficient motion performance in low Reynolds number environments, having great promise for biomedical applications like targeted delivery. However, during targeted delivery, the backward propulsion of MHMRs in previous work leads to cargo being released, limiting their degrees of freedom and interference resistance. Furthermore, the basic magnetic field parameter, amplitude, has not been effectively utilized in previous MHMRs. In this letter, we propose a magnetic helical miniature robot with soft magnetic-controlled gripper (MHMR-G), using magnetic field amplitude to functionalize MHMRs for the first time. The velocity of MHMR-G is controlled by magnetic field frequency and the grasping of gripper is controlled by magnetic field amplitude. It is proposed that the lag angle and rotation frequency will adversely affect the grasping of gripper under a rotating magnetic field, but results show that increasing magnetic field amplitude can effectively mitigate these adverse effects. Finally, a manipulation test of cargo transport is performed, demonstrating that the gripper of MHMR-G can effectively confine cargo during propulsion.**

***Index Terms*—Biologically-inspired robots, magnetic control, miniature robots, soft robotics.**

I. Introduction

UNTETHERED miniature robots can be propelled through various actuation fields [1], including magnetic fields, ultrasonic fields, light fields, etc. Compared to other actuation fields, magnetic fields have high tissue penetration, precise controllability and safe biocompatibility [1]. Furthermore, magnetic fields below 8T pose negligible risks to human health [2]. Consequently, magnetic miniature robots have emerged as a rapidly advancing frontier in the field of robots [3], [4], [5], and have great promise for biomedical applications [6], [7].

Manuscript received 2 October 2023; accepted 26 January 2024. Date of publication 14 February 2024; date of current version 22 February 2024. This letter was recommended for publication by Associate Editor Z. Zhang and Editor X. Liu upon evaluation of the reviewers' comments. This work was supported in part by China Postdoctoral Science Foundation under Grant 2021M690701, and in part by Guangdong Province Key Area Research and Development Program Project under Grant 2022B0303010001. *(Corresponding authors: Chenyao Bai; Yunlong Zhu.)*

Aoji Zhu, Chenyao Bai, Xiwen Lu, Yunlong Zhu, and Jiarui Zhu are with the Academy for Engineering and Technology, Fudan University, Shanghai 200433, China (e-mail: ajzhu21@m.fudan.edu.cn; baichenyao@fudan.edu.cn; xwlu21@m.fudan.edu.cn; zyl@fudan.edu.cn; 21210860025@m.fudan.edu.cn).

Kezhi Wang is with the Department of Computer Science, Brunel University London, UB8 3PH London, U.K. (e-mail: kezhi.wang@brunel.ac.uk).

This letter has supplementary downloadable material available at https://doi.org/10.1109/LRA.2024.3366018, provided by the authors.

Digital Object Identifier 10.1109/LRA.2024.3366018

In microscale or highly viscous environments, reciprocal swimmers are unable to achieve effective propulsion due to the low Reynolds number characteristics. Inspired by nature, Purcell demonstrated that prokaryotic organisms (e.g., E. coli [8]) can achieve effective propulsion in low Reynolds number environments by rotating their helical flagella [9]. In 1996, Honda et al. fabricated the first prototype of a magnetic helical microrobot in the world [10], [11]. In [12], three effective magnetic propulsion mechanisms in low Reynolds number environments were compared, and helical propulsion was considered the best choice in vivo applications. Due to the efficient torque drive strategy, magnetic helical miniature robots (MHMRs) require only a low-intensity magnetic field to achieve precise motion [13], making it a popular branch in the field of magnetic miniature robots. In recent years, the dynamic modeling of MHMRs has been discussed [14], and various control strategies have been applied to MHMRs [15], [16], [17], [18]. Also, novel designs and performance optimization of MHMRs have been proposed [19], [20], [21], [22]. In terms of applications, MHMRs have been experimentally verified in various biomedical scenarios, including targeted drug delivery [23], [24], blockage removal in vivo [25], [26], cellular cargo delivery [27], [28], etc.

In most biomedical scenarios, the payload capacity of MHMRs plays a crucial role. To address this, MHMRs with a gripper structure were designed in [29] to achieve stable cargo transport. However, the backward propulsion of MHMRs leads to the cargo being released from the gripper structure, which is unexpected for stable cargo transportation. Furthermore, the helical propulsion of MHMRs mainly utilized the frequency and orientation of rotating magnetic field in the previous literatures, but the amplitude, another key parameter of magnetic field, has not been well utilized for functional diversification of MHMRs.

Our motivation is to develop a MHMR with gripper that utilizes the magnetic field amplitude to prevent cargo release during transportation. Currently, various magnetic miniature robots with soft materials have been proposed [30], [31], [32], [33], [34], [35]. Among these, some gripper-shaped miniature robots that operate under the control of magnetic field amplitude give us a novel perspective. In [34], a novel untethered gripper composed of a magnetic elastic composite material was proposed for grasping. In [35], a new type of soft microrobot resembling a microgripper was proposed, which has two modes of motion under the varying magnetic field, either by tiny deformation or by rotation. However, compared to MHMRs, the motion of these soft magnetic miniature robots usually relies on magnetic field

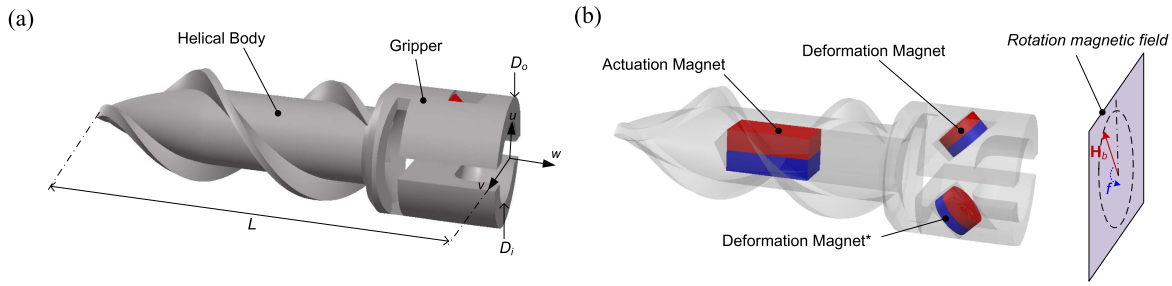

Fig. 1. MHMR-G configuration. (a) The three-dimensional model with the total length L, the outer diameter D_{o}, and the inner diameter D_{i}. (b) The distribution of embedded magnets in MHMR-G, including one actuation magnet and two deformation magnets. The MHMR-G rotates synchronously along with the rotating background magnetic field $\mathbf{H}_{\mathrm{b}}$ at the frequency f.

induced deformations and is mostly limited to planar motion, resulting in low motion performance.

In this letter, we propose a magnetic helical miniature robot with soft magnetic-controlled gripper (MHMR-G), of which the motion and grasping are both controlled by magnetic fields. Specifically, the MHMR-G retains the advantages of MHMRs, including efficient three-dimensional motion controlled by the frequency and orientation of rotating magnetic field. Moreover, it allows for the deformation control of gripper by varying the magnetic field amplitude. This ensures better cargo confinement during transportation, preventing unintended release. Through theoretical analyses, we derived three electromagnetic torques with distinct effects, leading to the propulsion, radial deformation and transverse deformation of MHMR-G. We validated the deformations under the magnetic field through simulations and experiments, assessing factors that could adversely affect the grasping of gripper. We also performed experiments to evaluate motion performance of MHMR-G under a rotating magnetic field, as well as a manipulation test of cargo transport.

The rest of the letter is organized as follows. In Section II, theoretical analyses of MHMR-G deformation and propulsion are conducted. In Section III, the fabrication of MHMR-G and magnetic actuation system are introduced. In Section IV, the simulation and experimental results are presented, followed by the concluding remarks in Section V.

II. Design and Modeling

The MHMR-G consists of its body and three embedded permanent magnets. The body can be divided into helical body and gripper. As shown in Fig. 1(a), a coordinate system is fixed at the front end of gripper, where the u-axis points in the direction of gripper releasing, the v-axis aligns with the symmetry plane of gripper, and the w-axis points along the rotating axis of MHMR-G. As shown in Fig. 1(b), the larger magnet embedded within the helical body is actuation magnet, serving as the primary actuating source for MHMR-G propulsion. Additionally, two other identical small magnets embedded within the gripper are deformation magnets. They are primarily used to deform the gripper and also serve as a partial actuating source for MHMR-G propulsion. When driven by a rotating background magnetic field $\mathbf{H}_{\mathrm{b}}$, the MHMR-G synchronously rotates and propels within the medium, with its velocity controlled by magnetic field frequency f. Furthermore, owing to the elastic material, the gripper can grasp and release the object by varying the magnetic field amplitude H_b.

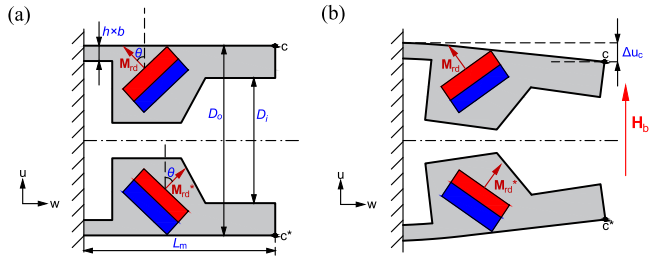

Fig. 2. Gripper deformation under a static magnetic field $\mathbf{H}_{\mathrm{b}}$. (a) Initial state of gripper in uw-plane, where D_{o} is the outer diameter, D_{i} is the inner diameter, $h \times b$ represents the thickness and width of support cross-section, L_{m} is the length of gripper, and θ is the angle between the remanent magnetization and u-axis. The remanent magnetization of two symmetrical deformation magnets M_{rd} and $\mathrm{M}_{\mathrm{rd}}^*$ have same amplitude but different directions. (b) After deformation, the displacement of point c along u-axis is Δu_{c}.

A. Gripper Deformation Under Static Magnetic Field

Under a static background magnetic field, the deformation of gripper is more convenient for analysis and experimental evaluation. Fig. 2 illustrates the deformation of the gripper in uw-plane under a static background magnetic field $\mathbf{H}_{\mathrm{b}}$. The remanent magnetization of deformation magnet forms an angle θ with the orientation of background magnetic field $\mathbf{H}_{\mathrm{b}}$. Due to symmetry, we can just analyze one deformation magnet. As the amplitude of background magnetic field H_b gradually increases, the remanent magnetization of deformation magnet $\mathbf{M}_{\mathrm{rd}}$ tends to align with the orientation of background magnetic field, resulting in a grasping deformation, see Fig. 2(b). Conversely, by gradually decreasing the amplitude of background magnetic field, the cargo can be released by resilience of the elastic gripper.

The magnetization of permanent magnets with ferromagnetic properties exhibits a nonlinear relationship with background magnetic field [36]. However, when the magnetization is far below the magnetic saturation, it can be approximated as a linear relationship [37]. Hence, the magnetization of each deformation magnet in the gripper is given by:

$$\mathbf{M}_{\mathrm{d}} = \chi_m \mathbf{H} + \mathbf{M}_{\mathrm{rd}}, \tag{1}$$

where χ_m is the magnetization susceptibility of deformation magnet, $\mathbf{H} = \mathbf{H}_{\mathrm{b}} + \mathbf{H'}_{\mathrm{b}}$ and $\mathbf{H'}_{\mathrm{b}}$ is the background magnetic field generated by other embedded magnets in the vicinity. The

background magnetic field can exert electromagnetic torque and electromagnetic force on the deformation magnet. The magnetic torque of deformation magnet can be expressed as [37]:

$$\mathbf{T}_{\mathrm{d}} = \mu_0 V_{\mathrm{d}} \mathbf{M}_{\mathrm{d}} \times \mathbf{H}, \tag{2}$$

where V_{d} is the volume of deformation magnet and μ_0 is the permeability of vacuum. As the background magnetic field under consideration in this letter is a spatially uniform field without involving gradient fields, electromagnetic forces $\mathbf{F} = \mu_0 V_{\mathrm{d}} (\mathbf{M}_{\mathrm{d}} \cdot \nabla)\mathbf{H}$ [37] will not be considered.

When conducting deformation analysis on solid structures, it is common to employ the small deformation assumption to linearize the equilibrium equations. However, due to the significant deformation occurring in the gripper, it is necessary to consider the effects of geometric nonlinearity. In uvw coordinate, supposing that a point in gripper is $\mathbf{s} = (s_1, s_2, s_3)$, it moves to a new position $\mathbf{S} = \mathbf{s} + \mathbf{p}$ after deformation, where $\mathbf{p}$ is the displacement vector. The deformation can be described by the nonlinear Lagrangian strain tensor [38], which can be expressed as:

$$\varepsilon_{ij} = \frac{1}{2}\left(\frac{\partial p_i}{\partial s_j} + \frac{\partial p_j}{\partial s_i} + \frac{\partial p_k}{\partial s_i} \cdot \frac{\partial p_k}{\partial s_j}\right), \tag{3}$$

where i, j, k are index notations of the tensor and obey the Einstein summation convention [38]. The Second Piola-Kirchhoff stress works conjugate to the Lagrangian strain and they are often used in the deformation analysis of geometric nonlinearity. For the case where the elastic material is isotropic, the relationship between the Second Piola-Kirchhoff stress and the Lagrangian strain can be expressed by the Generalized Hooke's Law [38]:

$$\Sigma_{ij} = \frac{E}{1+\nu}\left(\varepsilon_{ij} + \frac{\nu}{1-2\nu}\varepsilon_{kk}\delta_{ij}\right), \tag{4}$$

where E is the Young's modulus, ν is the Poisson's ratio and δ_{ij} is the Kronecker delta symbol. In terms of the Second Piola-Kirchhoff stress, the balance of momentum can be expressed as [38]:

$$\rho_0 \frac{\partial^2 \mathbf{p}}{\partial t^2} = \rho_0 \mathbf{q} + \nabla_s [\mathbf{\Sigma} \cdot (\mathbf{I} + \nabla_s \mathbf{p})^T], \tag{5}$$

where ρ_0 is the density of undeformed gripper, $\mathbf{q}$ is the body force per unit volume like gravity or buoyancy force. By adding boundary load $\mathbf{T}_{\mathrm{d}}$ in (2) and fixed constraints, the displacement vector $\mathbf{p}$ of each point in gripper can be numerically solved.

B. Gripper Deformation and MHMR-G Rotation Under Rotating Magnetic Field

Actuated by a rotating background magnetic field, the MHMR-G rotates synchronously around w-axis. As shown in Fig. 1, the magnetic torque of actuation magnet $\mathbf{T}_a$ contributes entirely to the rotation of MHMR-G. Simultaneously, the magnetic torque component of deformation magnet projected onto uv-plane $\mathbf{T}_d^{\{uv\}}$ also contributes to the rotation of MHMR-G. For simplicity, the magnetized part of magnet $\chi_m \mathbf{H}$ and the unexpected background magnetic field $\mathbf{H}_b'$ are ignored. Thus, the amplitude of rotating magnetic torque $\mathbf{T}_{\mathrm{r}}$ around w-axis can

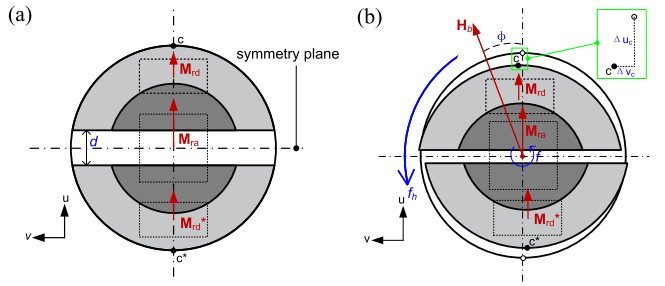

Fig. 3. Gripper deformation occurs when it rotates synchronously with a rotating background magnetic field $\mathbf{H}_{\mathrm{b}}$. (a) Initial state of gripper in uv-plane, where the dotted lines represent the locations of embedded magnets, d is the spacing of gripper and the red arrows represent the orientation of their remanent magnetization. (b) After deformation, the rotation frequency is $f_h = f$, and the lag angle is ϕ. The white and black points are the positions of c before and after deformation, respectively. After deformation, the radial and transverse displacements of point c are Δu_{c} and Δv_{c}.

be expressed as:

$$\mathrm{T_r} = \overbrace{\mu_0 V_{\mathrm{a}} \mathrm{H_b} \mathrm{M_{ra}} \sin(\phi)}^{by\ actuation\ magnet} + 2\overbrace{\mu_0 V_{\mathrm{d}} \mathrm{H_b} \mathrm{M_{rd}} \cos(\theta)\sin(\phi)}^{by\ deformation\ magnet}, \tag{6}$$

where V_{a} is the volume of actuation magnet, $\mathrm{M_{ra}}$ is the remanent magnetization of actuation magnet and ϕ is the lag angle by which the magnetization orientation of actuation magnet lags behind the background magnetic field during rotation, see Fig. 3(b). When the rotating magnetic torque and drag torque are balanced, the MHMR-G reaches synchronous rotation, thus obtaining:

$$\mathrm{T}_r = \tau = \xi f_h, \tag{7}$$

where ξ is the fluidic resistance coefficient describing the relationship between drag torque τ and rotation frequency f_h. When lag angle $\phi = 90^{\mathrm{o}}$, $\mathbf{T}_r$ reaches the maximum value, and then the MHMR-G reaches the maximum rotation frequency, also known as the step-out frequency f_{stepout} [14]. Therefore, the relationship between the rotation frequency of MHMR-G and background magnetic field can be expressed as:

$$\begin{cases} f_h = f, & f \le f_{\mathrm{stepout}} = \{\mathrm{T}_r\}_{\max}/\xi \\ f_h \ne f, & f > f_{\mathrm{stepout}} \end{cases}. \tag{8}$$

According to equations (6) and (7), when $f \le f_{\mathrm{stepout}}$, the relationship between the lag angle and the magnetic field frequency can be expressed as follows:

$$\frac{\sin(\phi)}{\sin(90^{\mathrm{o}})} = \frac{f}{f_{\mathrm{stepout}}}. \tag{9}$$

The deformation of gripper under a rotating magnetic field can be divided into radial deformation and transverse deformation. As shown in Fig. 3, the center points c and c* of gripper are displaced during deformation. The radial displacement toward the symmetry plane Δu_{c} is produced by the magnetic torque component of deformation magnet projected onto uw-plane $\mathbf{T}_d^{\{uw\}}$, which is the desired effect. Thus, the amplitude of radial deformation magnetic torque $\mathbf{T}_{\mathrm{dr}}$ can be expressed as:

$$\mathrm{T_{dr}} = \mu_0 V_{\mathrm{d}} \mathrm{H_b} \mathrm{M_{rd}} \sin(\theta)\cos(\phi). \tag{10}$$

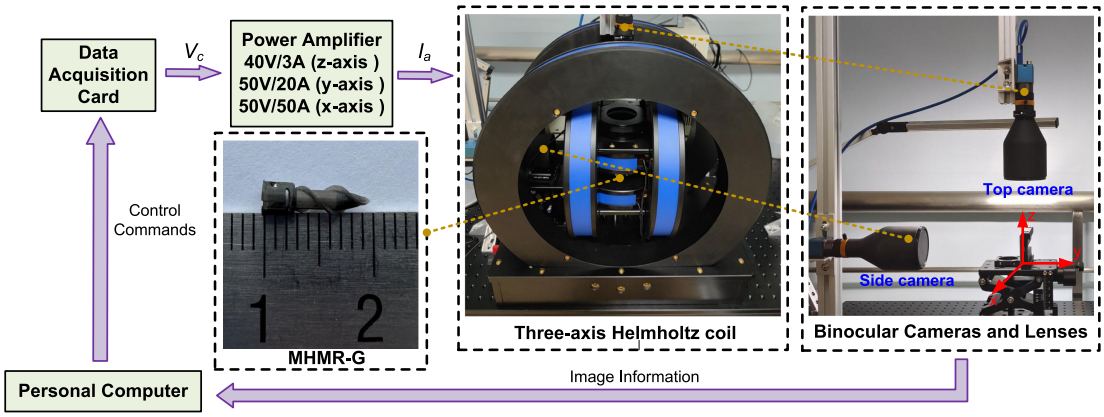

Fig. 4. Magnetic actuation system and MHMR-G prototype. The world coordinate system xyz is fixed at the center point of the three-axis Helmholtz coil, with each axis pointing in the direction of the corresponding coil axis.

The transverse displacement in the direction parallel to the symmetry plane Δv_{c} is is produced by the magnetic torque component of deformation magnet projected onto vw-plane $\mathbf{T}_d^{\{vw\}}$, which is an undesired effect, and will cause the dislocation of gripper. The amplitude of transverse deformation magnetic torque $\mathbf{T}_{\mathrm{dt}}$ can be expressed as:

$$\mathrm{T_{dt}} = \mu_0 V_{\mathrm{d}} \mathrm{H_b} \mathrm{M_{rd}} \sin(\theta)\sin(\phi). \tag{11}$$

The radial and transverse deformation magnetic torques act on the two deformation magnets respectively, with the same amplitude and opposite direction, resulting in grasping deformation and dislocation of the gripper.

The MHMR-G is relatively stationary with the magnetic field during synchronous rotation, so equation (5) can still be used to describe the deformation of gripper during rotation. However, the body force per unit volume $\mathbf{q}$ needs to additionally consider the effect of centripetal force, and the boundary load will be replaced by $\mathbf{T}_r$ and $\mathbf{T}_d$. Although the transverse deformation and centripetal force may have unfavorable effects on the grasping during MHMR-G rotation, their influence is minimal or can be effectively controlled and we will discuss these impacts in Section IV-B.

C. Helical Propulsion Under Rotating Magnetic Field

The helical structure of MHMR-G allows it to convert rotational motion into helical propulsion, with the direction of propulsion controlled by the orientation of rotating background magnetic field. When the frequency is low, the MHMR-G will wobble because its rotating axis and forward direction do not align well. As the frequency increases, the rotating axis aligns better with the forward direction, eliminating the wobbling phenomenon [13]. However, when the frequency further increases and reaches the step-out frequency, the MHMR-G will no longer be able to propel effectively. Within the effective propulsion region, the velocity of MHMR-G is linearly proportional to the frequency of rotating background magnetic field [13], [39] and can be expressed as:

$$v = \frac{-b}{a+\Psi} f, \ f_w \le f \le f_{\mathrm{stepout}}, \tag{12}$$

TABLE I
VALUES OF EXPERIMENTAL CONFIGURATION PARAMETERS

Parameter	Denotation	Value
Length of MHMR-G	L [mm]	10
Outer Diameter of gripper	D_{o} [mm]	3
Inner Diameter of gripper	D_{i} [mm]	1.9
Length of gripper	L_{m} [mm]	3.1
Support Cross-section Size	$h \times b$ [mm]	0.2×1.2
Angle of Deformation Magnet	θ [°]	45
Spacing of gripper	d [mm]	0.5
Size of Actuation Magnet	[mm]	$1 \times 1 \times 2$
Size of Deformation Magnet	[mm]	D1 $\times$ 0.5
Young's Modulus of F80	E [MPa]	1.8
Density of F80	[kg/m^3]	1100
Density of Glycerol	ρ_m[kg/m^3]	1260
Viscosity of Glycerol [40]	η[Pa · s]	1.412(20°C)
Spacing Between Coils (x,y,z-axis)	[mm]	215, 140, 80
Diameter of Coils (x,y,z-axis)	[mm]	430, 280, 160
Number of Coil Turns (x,y,z-axis)	-	55, 90, 326
Gain Coefficient (x,y,z-axis)	K_a[A/V]	19, 7.4, 1.4
Transfer Coefficient (x,y,z-axis)	K_b [mT/A]	0.22, 0.54, 3.38

where a and b are related to the geometric characteristics of helical structure, Ψ is related to the other part of MHMR-G, like the gripper in this letter, f_w is the minimum frequency to get out of the wobbling region. Therefore, the propulsion velocity of MHMR-G can be controlled by magnetic field frequency f.

III. SYSTEM CONFIGURATIONS

A. Fabrication of MHMR-G

The MHMR-G was fabricated using digital light processing (DLP) 3D printing technology. The printing equipment is PTM-5 from Shenzhen Phenix Tech, and the material used is F80 elastic resin from Resione. The prototype of MHMR-G is shown in Fig. 4, with approximate dimensions of 10 mm $\times$ 3 mm. The magnets are manually embedded in the MHMR-G and are made of NdFeB material with an N52 grade. Detailed parameters and materials of MHMR-G are provided in Table I.

B. Magnetic Actuation System

Since the Helmholtz coil can generate a highly uniform magnetic field linearly related to input current in the central region [2], helping to improve control performance, a three-axis

Helmholtz coil system is employed as the source of background magnetic field. As shown in Fig. 4, the vision system uses top and side cameras to position and track MHMR-G through image information. The camera used is model MER2-160-227U3M/C from Daheng Imaging, and the lens used is model GCO-232106 from Daheng Optics. The QT program on the personal computer sends control commands to the data acquisition card based on the image information, and then inputs voltage V_c to the power amplifiers of each axis, respectively. The data acquisition card used is model USB3155 from ART technology. Three pairs of coils define the x-axis, y-axis, and z-axis of world coordinate system, and the maximum currents for power amplifiers of the three axes are 50 A (x-axis), 20 A (y-axis), and 3 A (z-axis), respectively. After applying current I_a to the coil, each axis can generate a uniform magnetic field with a maximum of 10 mT. The working space of the coil is approximately a spherical region centered at the coil center with a diameter of 60 mm. The variation rate of the magnetic field within this spherical region is less than 5%.

The control scheme employed is a straightforward open-loop gain control. The control input is the voltage V_c from the data acquisition card, and the resulting magnetic field B_b is given by $B_b = K_a K_b V_c$, where $B_b = \mu_0 H_b$, K_a is the gain coefficient of the power amplifier, and the transfer coefficient K_b describes the linear relationship between input current and magnetic field, calibrated using the Gaussmeter. Since this letter does not involve complex control experiments, the accuracy of the open-loop control is already sufficient. Detailed parameters of the actuation system are provided in Table I.

C. Generation of Rotating Magnetic Field

A rotating magnetic field in any orientation can be obtained by combining the magnetic field components generated by the orthogonally Helmholtz coils. First, consider a base magnetic field, such as a rotating magnetic field rotating around the z-axis $\mathbf{B}_{\mathrm{b}}^{(0,0,1)} = [B_b \cos(2\pi f t),\ B_b \sin(2\pi f t),\ 0]^T$. Rotating the z-axis to any orientation can be represented by a rotation matrix $\mathbf{R}$ composed of three Euler angles α, β and γ, i.e., $[e_1, e_2, e_3]^T = \mathbf{R}_{\{\alpha\beta\gamma\}}[0, 0, 1]^T$. Therefore, the rotating magnetic field in any orientation can be expressed as:

$$\mathbf{B}_{\mathrm{b}}^{(e_1,e_2,e_3)} = \begin{bmatrix} \mathrm{B}_x \\ \mathrm{B}_y \\ \mathrm{B}_z \end{bmatrix} = \mathbf{R}_{\{\alpha\beta\gamma\}} \begin{bmatrix} B_b \cos(2\pi f t) \\ B_b \sin(2\pi f t) \\ 0 \end{bmatrix}, \qquad (13)$$

where B_x, B_y and B_z are the magnetic field components generated by x-axis, y-axis, and z-axis coils, respectively. Compared to H_b, B_b can be more conveniently detected in practical scenarios. Therefore, in Section IV, B_b is used instead of H_b to represent the background magnetic field.

IV. Results and Discussion

A. Deformation Results Under Static Magnetic Field

Studying the deformation of MHMR-G under a static magnetic field can more intuitively reflect the inherent factors affecting the cargo release of gripper. Due to the manufacturing process, the gripper of MHMR-G initially opens outward, resulting in a radial displacement $\Delta u_c < 0$. By applying a compensation magnetic field B_c (about 1mT), radial displacement can be corrected to $\Delta u_c = 0$, making the actual background magnetic field amplitude $B_b = B_c + \Delta B_b$. As shown in Fig. 5, as the amplitude of background magnetic field increases, the gripper has remarkable gripping effect. Upon removing the background magnetic field, the gripper releases quickly, see attached video. Then, a total of 6 sets of data were tested, and the experimental results are shown in Fig. 6(b), and (c). When B_b reaches 9 mT, the gripper reaches the maximum radial displacement $\Delta u_c + \Delta u_c^* \approx d$.

The deformation simulation of MHMR-G under a static magnetic field is conducted in COMSOL, utilizing the solid mechanics module and the electromagnetic fields module, and the simulation configuration refers to Section II and Table I. As shown in Fig. 6(a), the deformation trend in the simulation is consistent with the experimental test results. For a more intuitive understanding, we define the relative radial displacement as $Ru_c = (\Delta u_c + \Delta u_c^*)/d$ and the relative transverse displacement as $Rv_c = (\Delta v_c + \Delta v_c^*)/d$, respectively. Next, the effects of intrinsic parameters h and E on the radial displacement are investigated because they are the most important parameters affecting the the grasping of gripper, and the simulation results are shown in Fig. 6(b) and (c). When the background magnetic field is zero, the simulation curves all exhibit an initial radial displacement, which is generated by the mutual interaction between magnets within MHMR-G. Furthermore, it also indicate that reducing the cross-section thickness h of MHMR-G and the Young's modulus E of material both lead to an increase in radial displacement. Therefore, h and E can be used as parameters to adjust the grasping capability of gripper. The radial displacement in experimental results approaches zero in the initial state due to the compensation magnetic field, and the curves of experimental results and simulation results generally tend to fit in Fig. 6(b) and (c).

B. Deformation Results Under Rotating Magnetic Field

Compared with static magnetic field, the deformation of MHMR-G under a rotating magnetic field needs to consider the external factors caused by rotation, i.e., the lag angle ϕ and rotation frequency f. The lag angle ϕ leads to a radial displacement attenuation and generates undesired transverse displacement. Also, the centripetal force caused by rotation frequency results in a radial displacement attenuation. Since the rotation speed of MHMR-G is synchronized with the background magnetic field, it can be considered relatively stationary in the deformation simulation.

The four lines in Fig. 7(a) and (b) represent the simulation results of radial and transverse displacements with varying lag angles at $f = 6$ Hz. When the lag angle ϕ increases, the radial displacement of gripper gradually decreases and tends to zero at the maximum angle 90^o, while the transverse displacement gradually increases. According to the torque balance (6) and (7), when the rotation frequency is constant, it satisfies $B_b \sin(\phi) = \mathrm{const}$. In the experiments conducted in Section IV-C, we measured that the step-out frequency of MHMR-G is approximately 24 Hz under $B_b = 10$ mT. According to equation (9) and

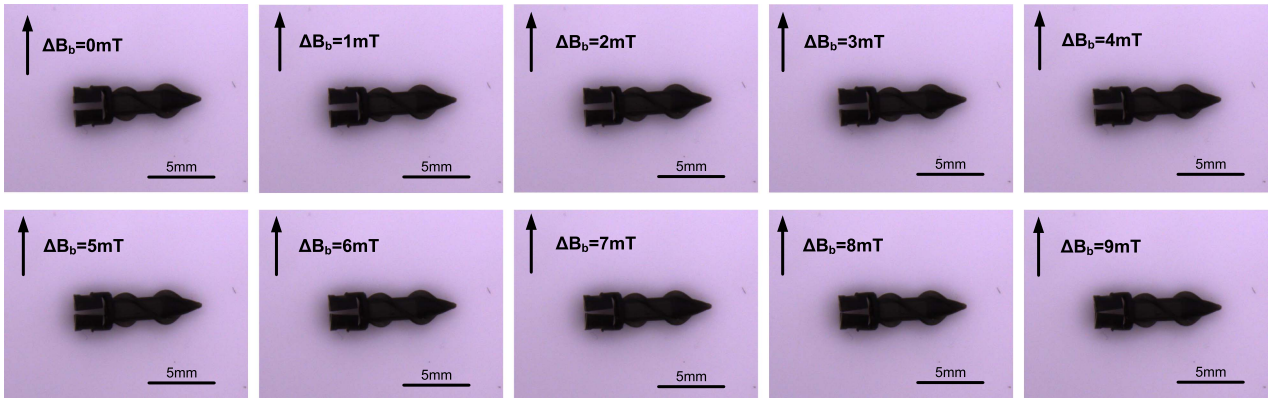

Fig. 5. Experimental demonstrations of MHMR-G deformation under a static magnetic field.

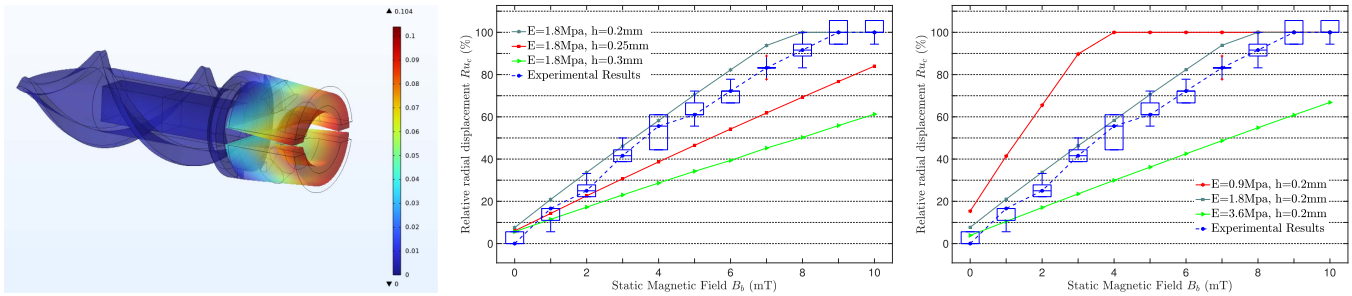

(a) (b) (c)

Fig. 6. Results of MHMR-G deformation under static magnetic field. (a). Illustration in COMSOL software. (b). The comparison of radial displacement experimental results and simulation results for different cross-section thickness h, with varying static magnetic field amplitude B_b. (c). The comparison of radial displacement experimental results and simulation results for different Young's modulus E, with varying static magnetic field amplitude B_b.

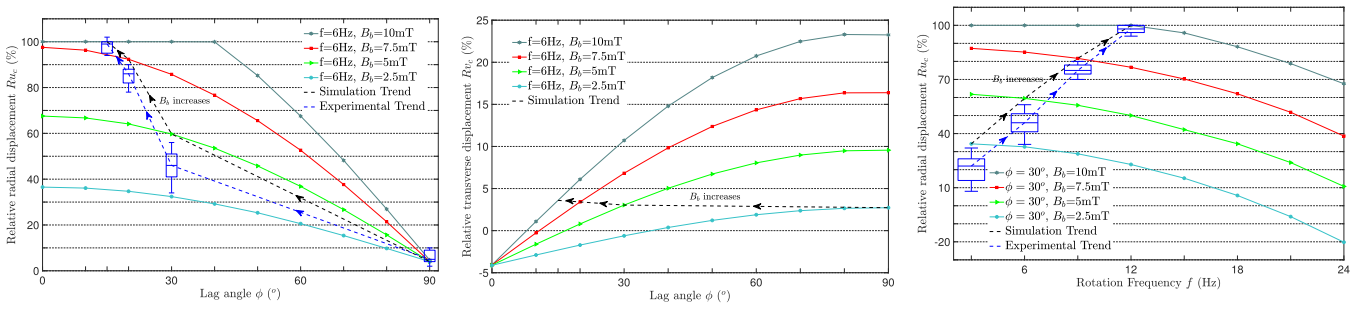

(a) (b) (c)

Fig. 7. Results of MHMR-G deformation under rotating magnetic field. (a). The comparison of radial displacement simulation results for different rotating magnetic field amplitude B_b, with varying lag angle ϕ. (b). The comparison transverse displacement simulation results for different rotating magnetic field amplitude B_b, with varying lag angle ϕ. (c). The comparison of radial displacement simulation results for different rotating magnetic field amplitude B_b, with varying rotation frequency f.

$B_b sin(\phi) = \text{const}$, we can estimate that at $f = 6$ Hz, the corresponding lag angles for magnetic field amplitude of 2.5 mT, 5 mT, 7.5 mT, and 10 mT are approximately 90°, 30°, 20°, and 15°, respectively. The black dashed arrows in Fig. 7(a) and (b) show the simulation trends of radial and transverse displacements as the amplitude of background magnetic field B_b increases from 2.5 mT to 10 mT. It can be observed that the radial displacement significantly increases, while the transverse displacement remains relatively constant. In Section II-B, we have analyzed that the radial deformation torque (10) is proportional to $B_b \cos(\phi)$, and the transverse deformation torque (11) is proportional to $B_b \sin(\phi)$. Therefore, the simulation results are consistent with the theoretical analysis. Meanwhile, with the increase of the magnetic field, experimental results show a similar trend as simulation results in radial displacement, and some experimental footage can be found in the attached video. However, compared with the radial displacement, the transverse displacement is much smaller because the structural

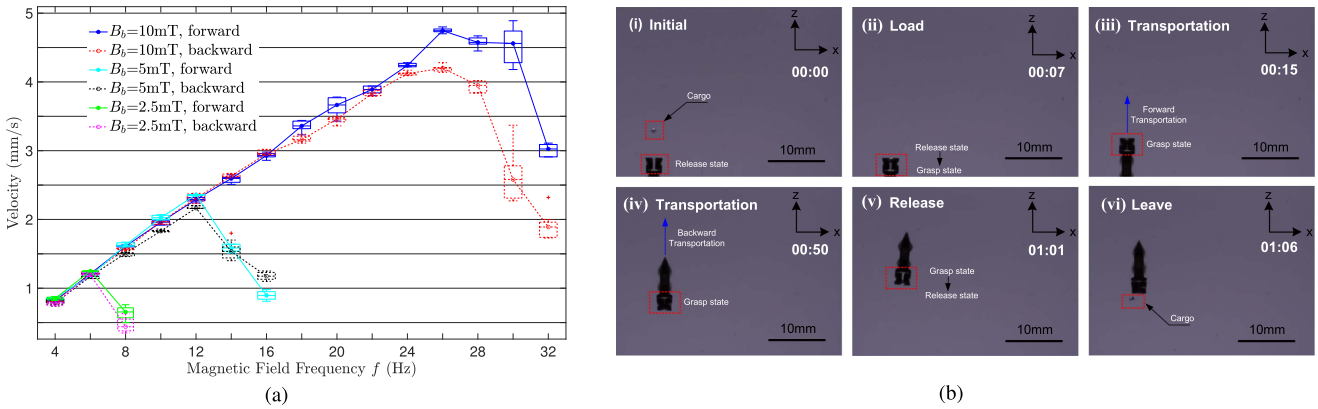

(a) (b)

Fig. 8. Results of MHMR-G propulsion in medium. (a). The experimental results of MHMR-G velocity for different rotating magnetic field amplitude B_b. (b). Experimental demonstrations of cargo transportation. Six frames captured by the side camera during experiment are shown in (i)–(vi). For detail, see the attached video.

design of MHMR-G is prone to radial deformation. It is challenging to effectively capture the experimental data, so only simulation results are provided in Fig. 7(b). According to the results, controlling frequency to make the lag angle $\phi \leq 30^o$ can ensure that the radial displacement is not weakened much and the transverse displacement can be approximately ignored. Therefore, increasing B_b is an effective way to limit the adverse effects of ϕ on grasping under rotating magnetic fields.

Since the centripetal force is proportional to the square of rotation frequency f, excessive rotation frequency will lead to a sharp decrease in the radial displacement of gripper. The four lines in Fig. 7(c) represent the simulation results of radial displacement with varying rotational frequency at a constant lag angle $\phi = 30^o$. Similarly, according to the experimental results in Section IV-C and (9), to maintain $\phi = 30^o$, the corresponding rotational frequencies for magnetic field amplitude of 2.5 mT, 5 mT, 7.5 mT, and 10 mT are approximately 3 Hz, 6 Hz, 9 Hz, and 12 Hz, respectively. Both simulation and experimental results consistently indicate that increasing B_b can effectively increase radial displacement. Therefore, increasing B_b is also an effective way to ensure that the adverse effects of centripetal force on grasping are limited under rotating magnetic fields.

C. Motion Performance of MHMR-G

In order to simulate a low Reynolds number environment at microscale, we used highly viscous glycerol as the medium for the motion MHMR-G. The motion velocity of MHMR-G ranges from 1–4 mm/s, and based on the experimental configuration parameters in Table I, the Reynolds number $Re = \frac{\rho_m v D_o}{\eta}$ can be calculated to be approximately 0.004–0.011, obviously indicating a low Reynolds number ($Re \ll 1$). The motion of the gripper at the front is defined as forward motion, while the motion of the gripper at the rear is defined as backward motion. We performed experiments on the forward and backward motion performance of MHMR-G and measured the velocity along x-axis to neglect z-direction shift caused by gravity. The experimental results are shown in Fig. 8(a), and some experimental footage can be found in the attached video. It can be seen that the velocity of MHMR-G is linearly related to magnetic field frequency f until reaching step-out frequency f_{stepout}, and the result is consistent with (12). Additionally, the step-out frequencys for forward and backward motion of MHMR-G are different but exhibit minimal variation. Furthermore, according to (8), the step-out frequency is positively correlated with B_b, which is also consistent with the experimental results.

D. Manipulation Test of Cargo Transport

We have performed a manipulation test on cargo transportation of MHMR-G. The six frames from side camera during the test are shown in Fig. 8(b), and the complete process is shown in attached video. The cargo used is a aluminum sphere with a diameter of 1 mm. In frame (i), the magnetic field is $B_b = 2.5$ mT and the frequency is $f = 5$ Hz, where MHMR-G is in a release state in preparation for cargo loading. In frame (ii), the magnetic field is increased to $B_b = 10$ mT, and the gripper generates radial deformation to confine the cargo. According to Section IV-C, when transporting cargo, the lag angle is best controlled within $\phi = 30^o$, which is reflected in the frequency that $f \leq 1/2 f_{\text{stepout}}$. Thus, in frame (iii), MHMR-G starts cargo transport at $B_b = 10$ mT and $f = 12$ Hz. In frame (iv), MHMR-G executes a backward motion, and the cargo does not fall out. The MHMR-G in frame (v) then removes the rotating magnetic field, causing the gripper to release, and the cargo falls out. Finally, MHMR-G restarts in frame (vi) and completes this cargo transport test.

V. Conclusion and Future Work

This letter introduces a magnetic helical miniature robot with soft gripper, capable of propulsion and grasping through adjustments in magnetic field frequency and amplitude. The deformation of gripper under a static magnetic field and a rotating magnetic field is analyzed theoretically and experimentally. The analysis derives three electromagnetic torques with distinct effects and identifies two factors that affect the grasping of gripper during dynamic motion, in particular, the lag angle and the rotation frequency. Results show that maintaining the

lag angle to be less than 30^o preserves radial displacement strength and mitigates undesired transverse displacement. It is also shown that increasing magnetic field amplitude effectively mitigates adverse effects induced by the lag angle and rotation frequency. Furthermore, a manipulation test of cargo transport demonstrates that the gripper of MHMR-G during propulsion can achieve effective grasping and release.

In the future, we will explore closed-loop control to enable MHMR-G to have autonomous tracking capabilities. Also, we hope to further reduce the size of MHMR-G, explore more materials and manufacturing processes, and investigate potential biomedical applications.

REFERENCES

[1] B. Wang, K. Kostarelos, B. J. Nelson, and L. Zhang, "Trends in micro-/nanorobotics: Materials development, actuation, localization, and system integration for biomedical applications," *Adv. Mater.*, vol. 33, no. 4, Jan. 2021, Art. no. 2002047.

[2] Z. Yang and L. Zhang, "Magnetic actuation systems for miniature robots: A review," *Adv. Intell. Syst.*, vol. 2, no. 9, Sep. 2020, Art. no. 2000082.

[3] H. Zhou, C. C. Mayorga-Martinez, S. Pané, L. Zhang, and M. Pumera, "Magnetically driven micro and nanorobots," *Chem. Rev.*, vol. 121, no. 8, pp. 4999–5041, Apr. 2021.

[4] L. Yang and L. Zhang, "Motion control in magnetic microrobotics: From individual and multiple robots to swarms," *Annu. Rev. Control, Robot., Auton. Syst.*, vol. 4, pp. 509–534, May 2021.

[5] J. Jiang, Z. Yang, A. Ferreira, and L. Zhang, "Control and autonomy of microrobots: Recent progress and perspective," *Adv. Intell. Syst.*, vol. 4, no. 5, May 2022, Art. no. 2100279.

[6] X. Du and J. Yu, "Image-integrated magnetic actuation systems for localization and remote actuation of medical miniature robots: A survey," *IEEE Trans. Robot.*, vol. 39, no. 4, pp. 2549–2568, Aug. 2023.

[7] B. J. Nelson, S. Gervasoni, P. W. Y. Chiu, L. Zhang, and A. Zemmar, "Magnetically actuated medical robots: An in vivo perspective," *Proc. IEEE*, vol. 110, no. 7, pp. 1028–1037, Jul. 2022.

[8] H. C. Berg and R. A. Anderson, "Bacteria swim by rotating their flagellar filaments," *Nature*, vol. 245, no. 5425, pp. 380–382, Oct. 1973.

[9] E. M. Purcell, "Life at low Reynolds number," *Amer. J. Phys.*, vol. 45, no. 1, pp. 3–11, Jan. 1977.

[10] T. Honda, K. Arai, and K. Ishiyama, "Micro swimming mechanisms propelled by external magnetic fields," *IEEE Trans. Magn.*, vol. 32, no. 5, pp. 5085–5087, Sep. 1996.

[11] F. Qiu and B. J. Nelson, "Magnetic helical micro-and nanorobots: Toward their biomedical applications," *Engineering*, vol. 1, no. 1, pp. 21–26, Mar. 2015.

[12] J. J. Abbott et al., "How should microrobots swim?," *Int. J. Robot. Res.*, vol. 28, no. 11/12, pp. 1434–1447, Nov. 2009.

[13] Y. Dong, L. Wang, V. Iacovacci, X. Wang, L. Zhang, and B. J. Nelson, "Magnetic helical micro-/nanomachines: Recent progress and perspective," *Matter*, vol. 5, no. 1, pp. 77–109, Jan. 2022.

[14] X. Wang, C. Hu, S. Pané, and B. J. Nelson, "Dynamic modeling of magnetic helical microrobots," *IEEE Robot. Automat. Lett.*, vol. 7, no. 2, pp. 1682–1688, Apr. 2022.

[15] H. Zhao, J. Leclerc, M. Feucht, O. Bailey, and A. T. Becker, "3D path-following using MRAC on a millimeter-scale spiral-type magnetic robot," *IEEE Robot. Automat. Lett.*, vol. 5, no. 2, pp. 1564–1571, Apr. 2020.

[16] J. Liu, T. Xu, and X. Wu, "Model predictive control of magnetic helical swimmers in two-dimensional plane," *IEEE Trans. Automat. Sci. Eng.*, early access, Mar. 07, 2023, doi: 10.1109/TASE.2023.3250701.

[17] R. Avaneesh, R. Venezian, C.-S. Kim, J.-O. Park, S. Misra, and I. S. M. Khalil, "Open-loop magnetic actuation of helical robots using position-constrained rotating dipole field," in *Proc. IEEE/RSJ Int. Conf. Intell. Robots Syst.*, 2021, pp. 8545–8550.

[18] T. Xu, J. Liu, C. Huang, T. Sun, and X. Wu, "Discrete-time optimal control of miniature helical swimmers in horizontal plane," *IEEE Trans. Automat. Sci. Eng.*, vol. 19, no. 3, pp. 2267–2277, Jul. 2022.

[19] L. Tan and D. J. Cappelleri, "Design, fabrication, and characterization of a helical adaptive multi-material microrobot (HAMMR)," *IEEE Robot. Automat. Lett.*, vol. 8, no. 3, pp. 1723–1730, Mar. 2023.

[20] J. E. Quispe, A. Bolopion, P. Renaud, and S. Régnier, "Enhancing swimming and pumping performance of helical swimmers at low Reynolds numbers," *IEEE Robot. Automat. Lett.*, vol. 6, no. 4, pp. 6860–6867, Oct. 2021.

[21] Y. Hou et al., "Design and control of a surface-dimple-optimized helical microdrill for motions in high-viscosity fluids," *IEEE/ASME Trans. Mechatronics*, vol. 28, no. 1, pp. 429–439, Feb. 2023.

[22] I. C. Yasa, H. Ceylan, U. Bozuyuk, A.-M. Wild, and M. Sitti, "Elucidating the interaction dynamics between microswimmer body and immune system for medical microrobots," *Sci. Robot.*, vol. 5, no. 43, Jun. 2020, Art. no. eaaz3867.

[23] H. Lee and S. Park, "Magnetically actuated helical microrobot with magnetic nanoparticle retrieval and sequential dual-drug release abilities," *ACS Appl. Mater. Interfaces*, May 2023.

[24] X. Wang et al., "Facile fabrication of magnetic microrobots based on spirulina templates for targeted delivery and synergistic chemo-photothermal therapy," *ACS Appl. Mater. Interfaces*, vol. 11, no. 5, pp. 4745–4756, Feb. 2019.

[25] J. Leclerc, H. Zhao, D. Bao, and A. T. Becker, "In vitro design investigation of a rotating helical magnetic swimmer for combined 3-D navigation and blood clot removal," *IEEE Trans. Robot.*, vol. 36, no. 3, pp. 975–982, Jun. 2020.

[26] S. Lee et al., "Fabrication and characterization of a magnetic drilling actuator for navigation in a three-dimensional phantom vascular network," *Sci. Rep.*, vol. 8, no. 1, pp. 1–9, Feb. 2018.

[27] M. Medina-Sánchez, L. Schwarz, A. K. Meyer, F. Hebenstreit, and O. G. Schmidt, "Cellular cargo delivery: Toward assisted fertilization by sperm-carrying micromotors," *Nano Lett.*, vol. 16, no. 1, pp. 555–561, Jan. 2016.

[28] S. Jeon et al., "Magnetically actuated microrobots as a platform for stem cell transplantation," *Sci. Robot.*, vol. 4, no. 30, May 2019, Art. no. eaav4317.

[29] S. Tottori, L. Zhang, F. Qiu, K. K. Krawczyk, A. Franco-Obregón, and B. J. Nelson, "Magnetic helical micromachines: Fabrication, controlled swimming, and cargo transport," *Adv. Mater.*, vol. 24, no. 6, pp. 811–816, Feb. 2012.

[30] H.-J. Chung, A. M. Parsons, and L. Zheng, "Magnetically controlled soft robotics utilizing elastomers and gels in actuation: A review," *Adv. Intell. Syst.*, vol. 3, no. 3, Mar. 2021, Art. no. 2000186.

[31] J. Zhang et al., "Voxelated three-dimensional miniature magnetic soft machines via multimaterial heterogeneous assembly," *Sci. Robot.*, vol. 6, no. 53, Apr. 2021, Art. no. eabf0112.

[32] S. Yuan et al., "Versatile motion generation of magnetic origami spring robots in the uniform magnetic field," *IEEE Robot. Automat. Lett.*, vol. 7, no. 4, pp. 10486–10493, Oct. 2022.

[33] J. Cui et al., "Nanomagnetic encoding of shape-morphing micromachines," *Nature*, vol. 575, no. 7781, pp. 164–168, Nov. 2019.

[34] J. Zhang and E. Diller, "Tetherless mobile micrograsping using a magnetic elastic composite material," *Smart Mater. Struct.*, vol. 25, no. 11, Nov. 2016, Art. no. 11LT03.

[35] M. Su, T. Xu, Z. Lai, C. Huang, J. Liu, and X. Wu, "Double-modal locomotion and application of soft cruciform thin-film microrobot," *IEEE Robot. Automat. Lett.*, vol. 5, no. 2, pp. 806–812, Apr. 2020.

[36] D. J. Griffiths, *Introduction to Electrodynamics*. London, U.K.: Cambridge Univ. Press, 2005.

[37] J. J. Abbott, O. Ergeneman, M. P. Kummer, A. M. Hirt, and B. J. Nelson, "Modeling magnetic torque and force for controlled manipulation of soft-magnetic bodies," *IEEE Trans. Robot.*, vol. 23, no. 6, pp. 1247–1252, Dec. 2007.

[38] A. F. Bower, *Applied Mechanics of Solids*. Boca Raton, FL, USA: CRC press, 2009.

[39] K. E. Peyer, L. Zhang, and B. J. Nelson, "Bio-inspired magnetic swimming microrobots for biomedical applications," *Nanoscale*, vol. 5, no. 4, pp. 1259–1272, May 2013.

[40] J. B. Segur and H. E. Oberstar, "Viscosity of glycerol and its aqueous solutions," *Ind. Eng. Chem.*, vol. 43, no. 9, pp. 2117–2120, Sep. 1951.